

## Article

# Microstructure and Mechanical Properties of $Ti-TiH_2$ Based Matrix Composites Reinforced with $xTiB_2$ Particles Processed by Powder Metallurgy

David Israel Bravo Barcenas <sup>1</sup>, Jorge Manuel Chávez Aguilar <sup>2</sup> , Omar Jiménez Alemán <sup>3,\*</sup> , Luis Olmos Navarrete <sup>4</sup> , Max Fernando Flores Jiménez <sup>1</sup>, Marco Aurelio González Albarrán <sup>1</sup> and Iván Gerardo Farias Velázquez <sup>3</sup>

<sup>1</sup> Departamento de Ingeniería de Proyectos, Centro Universitario de Ciencias Exactas e Ingenierías, CUCEI, CONACyT-Universidad de Guadalajara, José Guadalupe Zuno #48, Los Belenes, Zapopan C.P. 45100, Jalisco, Mexico

<sup>2</sup> Departamento de Ingeniería Mecánica Eléctrica, Centro Universitario de Ciencias Exactas e Ingenierías, CUCEI, Universidad de Guadalajara, Blvd. Marcelino García Barragan #1421, Guadalajara C.P. 44430, Jalisco, Mexico

<sup>3</sup> Departamento de Ingeniería de Proyectos, Centro Universitario de Ciencias Exactas e Ingenierías, CUCEI, Universidad de Guadalajara, José Guadalupe Zuno #48, Los Belenes, Zapopan C.P. 45100, Jalisco, Mexico

<sup>4</sup> Instituto de Investigaciones en Ciencias de la Tierra, INICIT, Universidad Michoacana de San Nicolás de Hidalgo, Ciudad Universitaria, Av. Francisco J. Mujica S/N, Edificio U-3, Morelia C.P. 58030, Michoacan, Mexico

\* Correspondence: omar.aleman@academicos.udg.mx



**Citation:** Bravo Barcenas, D.I.; Chávez Aguilar, J.M.; Jiménez Alemán, O.; Olmos Navarrete, L.; Flores Jiménez, M.F.; González Albarrán, M.A.; Farias Velázquez, I.G. Microstructure and Mechanical Properties of  $Ti-TiH_2$  Based Matrix Composites Reinforced with  $xTiB_2$  Particles Processed by Powder Metallurgy. *Coatings* **2023**, *13*, 587. <https://doi.org/10.3390/coatings13030587>

Academic Editor: German Prieto

Received: 1 February 2023

Revised: 25 February 2023

Accepted: 1 March 2023

Published: 9 March 2023



**Copyright:** © 2023 by the authors. Licensee MDPI, Basel, Switzerland. This article is an open access article distributed under the terms and conditions of the Creative Commons Attribution (CC BY) license (<https://creativecommons.org/licenses/by/4.0/>).

## 1. Introduction

In recent years, sintered titanium-based alloys have been widely used for aerospace and biomedical applications because of their appropriate properties such as low density, high strength, resilience, high toughness, low Young modulus, excellent corrosion resistance, and biocompatibility [1–5]. Therefore, researchers have developed alternative PM methodologies with the purpose to fabricate titanium alloys with a significant cost-affordable reduction, as compared to existing technologies, by decreasing the consumption of CP titanium without degradation of their properties [6–11].

The obtaining of low-cost raw *Ti* materials by using *TiH<sub>2</sub>* as a Ti source is considered a viable way to fabricate several types of devices, promoting its usage in several applications. This processing is benefited by the use of hydrogen, which enhances the processability of *Ti*, including cold and hot working, machining, superplastic forming, and microstructure control for the improvement of the mechanical properties [7,8,12–14]. The use of amounts higher than 3 wt.% of *TiH<sub>2</sub>* instead of conventional *Ti* powder significantly improves sintering, providing almost full density to the final component, and better homogeneity of fabricated alloys [7,12,14,15].

On the other hand, an efficient method to improve the mechanical properties of titanium alloys is the addition of hard ceramic particles as reinforcement, such as titanium nitrides [16,17], carbides [17,18], and borides [17–19]. These reinforcing particles have been used due to their higher mechanical properties. Such reinforcements can be also produced by the in situ reaction, using solid or gaseous precursors, resulting in the formation of hard precipitates [16–19]. Focusing on *TiB<sub>2</sub>*-reinforced titanium-based alloys, it was found that composite materials have been manufactured from solid precursors using mixtures of *Ti-B*, *Ti-BC*, *Ti-CrB*,  $(Ti)_x(TiB)_{1-x}$  or *Ti-B<sub>4</sub>C* powders. These composites are usually fabricated through different PM processing techniques, which include Spark Plasma Sintering (SPS) [20], Pseudo Hot Isostatic Pressing (PHIP) [21], Reactive Hot Pressing (RHP) [22,23], Hot Isostatic Pressing (HIP) [24], and Self Propagating High-Temperature Synthesis (SHS) [21]; those powder-based routes provide good microstructural control and a minimal amount of wasted raw materials. The volume fraction of *TiB<sub>2</sub>* generates changes in the elastic properties, residual stresses, stiffness, and chemical stability of titanium-based sintered alloys [22,25,26]. Hence, to reinforce effectively a *Ti* matrix, it was recommended to produce *TiB* whiskers in proportions in the range of 0.1–10 volume fraction, because it requires a lower amount of B for the formation and offers ease of manufacturing [24,27]. Morsi and Patel [19] reported that *TiB* whiskers formation can be favored using boron sources such as *TiB<sub>2</sub>*, *B*, *CrB*, *MoB*, or other compounds that contain *Ti* phase stabilizers; through the stable chemical reaction between both the *Ti* matrix and the boron source. Moreover, it has been demonstrated that the formation of *TiB* whiskers is achieved by having a boron concentration of less than 18 wt.%, when there is an excess of *Ti* and having enough time to allow diffusion phenomena [8,18,28,29].

In this investigation, the microstructure and mechanical properties of a *Ti-TiH<sub>2</sub>* matrix reinforced with *TiB<sub>2</sub>* ceramic particles were studied. Composites were sintered by the PM process, using high vacuum conditions. The effects of the addition of the *TiB<sub>2</sub>* particles on the formation of the microstructure of the *Ti-TiH<sub>2</sub>* matrix were studied by FE-SEM, EDS, and XRD. Additionally, the effect of the volume fraction of reinforcing particles on the mechanical and elastic properties was evaluated to provide greater resolution on the combined properties of the compounds and assess their potential for orthopedic applications.

## 2. Materials and Methods

Spherical CP-*Ti* Grade 1 powder with particle size < 45 µm (Raymor AP&C), irregular *TiH<sub>2</sub>* grade VM with particle size < 8 µm (Chemetall, Frankfurt, Germany), and irregular *TiB<sub>2</sub>* particles with size < 10 µm (Sigma-Aldrich, Burlington, MA, USA) powders were used in this study. The raw materials used for this research were analyzed by using a scanning electron microscope MIRA 3 LMU TESCAN (Warrendale, PA, USA), and an X-ray Diffractometer Empyrean PANalytical (Malvern, UK). *Ti* and *TiH<sub>2</sub>* powders for the matrix were mixed in a 1:1 ratio. Then, amounts of 0, 3, 10, and, 30 vol.% of *TiB<sub>2</sub>* particles were added as reinforcement. Mixtures were poured into a sealed polyethylene container. This action was carried out in a purged gloves chamber to prevent the oxidation of powders. Subsequently, the powders were mixed in a turbula at 75 rpm for 5 h to obtain homogeneous mixtures. Cylindrical green samples of 12 mm diameter and 10 mm height were obtained by compacting the powders using a graphite die with a constant pressure of 442 MPa. Green compacts were consolidated by using sintering in high vacuum condition ( $10^{-6}$  mbar), into a BREW furnace. During the sintering cycle, the dehydrogenation of *TiH<sub>2</sub>*

was performed at 550 °C for 1 h. A heating rate of 5 °C·min<sup>-1</sup> was employed during processing. The dehydrogenation process was repeated at 700 °C, for 1 h, in order to ensure the complete dehydrogenation of powders. Finally, the samples were sintered at three different temperatures: 850, 1100, and 1300 °C with a dwell time of 2 h. The cooling of the samples was carried out inside the furnace. After sintering, samples were ultrasonically cleaned in acetone and deionized water, each for 15 min at room temperature, and then dried and stored under a clean desiccator chamber. Table 1 shows the designation for samples used within this study, concerning the  $TiB_2$  particle content and sintering temperature.

**Table 1.** Nominal content and designation samples, for the set of experimental sintering conditions.

Sample	Designation	$TiB_2$ Particles (vol.%)	Sintering Temperature (°C)
Unreinforced	U-a		850
	U-b	0	1100
	U-c		1300
Reinforced	R3-a		850
	R3-b	3	1100
	R3-c		1300
	R10-a		850
	R10-b	10	1100
	R10-c		1300
	R30-a		850
	R30-b	30	1100
	R30-c		1300

The relative density of sintered samples was estimated from their weight and dimensions (volume), determining the measured density and relating it to the theoretical density, which was calculated by the rule of mixtures using Equation (1).

$$\rho_C = \rho_m f_m + \rho_r f_r \quad (1)$$

where  $\rho_C$ ,  $\rho_m$  and,  $\rho_r$  are the weight densities of the composite, the matrix particles, and the reinforcement particles, respectively, while  $f_m$  and  $f_r$  are the volume fractions of the matrix and the reinforcement particles, respectively.

Sintered samples were cross-sectioned for metallographic preparation by roughing with SiC sandpaper with grain size from 180 to 2000 grit and polishing with 3 and 1 microns alumina solution. Final polishing was performed with 0.05 and 0.02 microns of non-crystallizing colloidal silica suspension. Polished samples were chemically etched with Kroll's reagent, composed of 100 mL distilled H<sub>2</sub>O, 6 mL HNO<sub>3</sub>, and 3 mL HF, by immersion for 120 s. The microstructure of the surface and topography of the sintered samples were observed using a Nikon ECLIPSE MA optical microscope and a MIRA 3MLU TESCAN Field-Emission scanning electron microscope. The structure analysis of materials was characterized by XRD employing a PANalytical Empyrean Difactometer using CuK $\alpha$  radiation of  $\lambda = 0.154$  nm and a scan rate of 0.026°·s<sup>-1</sup> in a 2 $\theta$  range of 20–90°. The presence of secondary elements was examined by using an elemental analyzer X-ray Energy Dispersion Spectrometry (EDS) instrument XFlash 6|30 Detector Bruker (Billerica, MA, USA). Reticular parameters were calculated following Cohen's method [30], and crystallite sizes were determined by modifying Scherrer's equation [31].

The effect of the addition of the  $TiB_2$  particles on the elastoplastic properties and microhardness of the composites was measured using nanoindentation techniques and microhardness Vickers tests. Nanoindentations were performed using a NANOVEA CB500

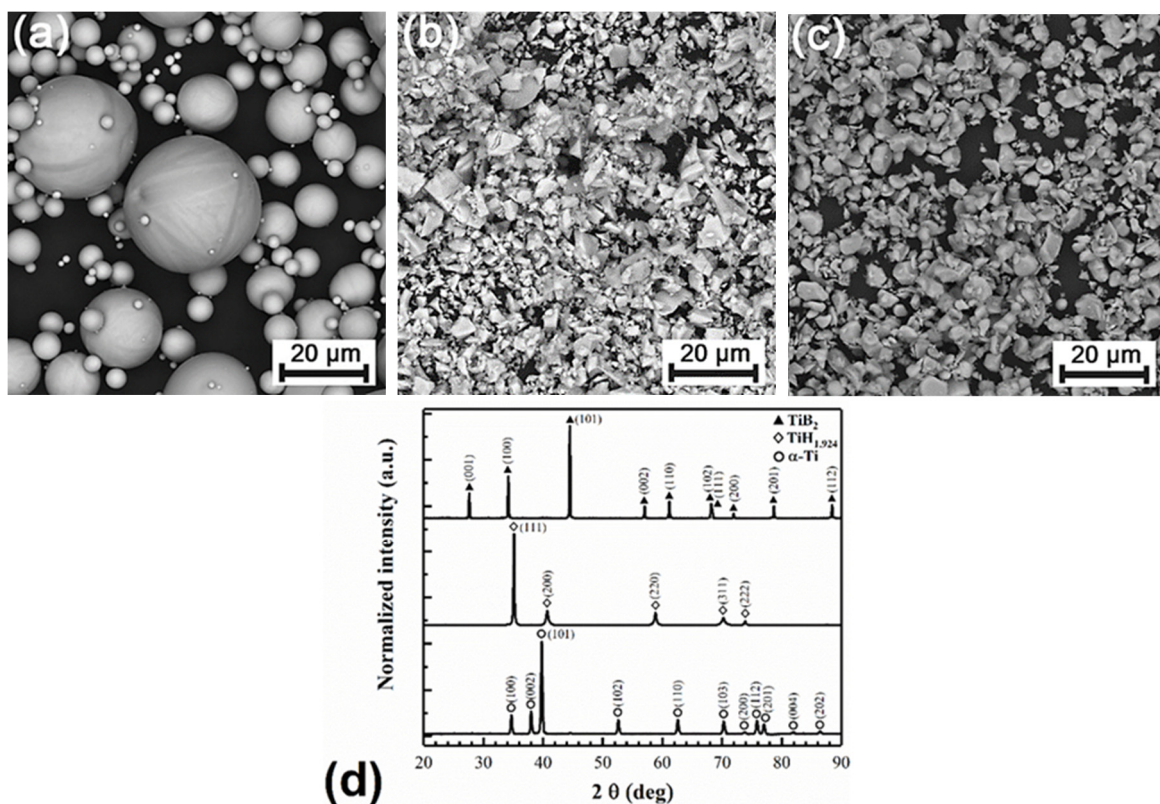
nanoindenter (Irvine, CA, USA) on the polished cross-section surface of the samples with a constant applied load of 50 mN ( $P_{max}$ ). A total of 25 indentations using a  $5 \times 5$  matrix pattern were achieved. The recorded load-depth curves were analyzed according to the Oliver-Pharr procedure [32] in order to assess the evolution of the hardness. The hardness values were then obtained by considering the projected area of the Berkovich print and the contact indentation depth ( $h_c$ ) using Equation (2).

$$H = P_{max} / 24.5h_c^2 \quad (2)$$

The reduced Elastic modulus ( $E_r$ ) was estimated. The average value of 25 indentations was used for the estimation of  $H$  and  $E_r$  for the samples. Vickers microhardness tests were carried out on the cross-section of the samples using a constant load of 98 mN with a dwell time of 15 s using a microhardness tester Future-Tech FM-800. A total of 10 microindentations per sample were used to obtain the average values of the hardness of materials.

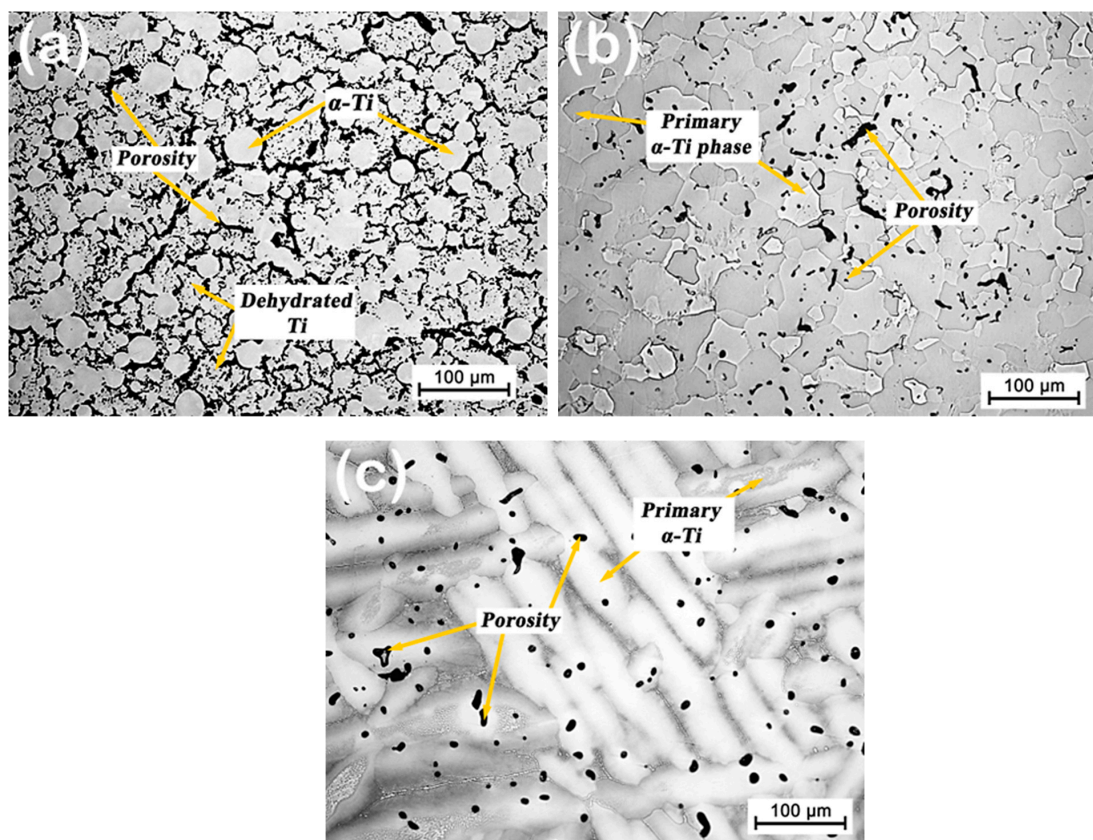
### 3. Results and Discussions

Figure 1 shows SEM micrographs and XRD patterns for the as receive raw powders. Figure 1a shows powders with a spherical morphology corresponding to CP-Ti Grade 1, Figure 1b exhibits an irregular  $TiH_2$  powder and Figure 1c shows asymmetrical  $TiB_2$  reinforcement particles. XRD patterns of the as-received powders are shown in Figure 1d. CP-Ti powders consisted of the  $\alpha$ -Ti phase with a hexagonal structure of the P63/mmc space group while  $TiB_2$  powders presented a hexagonal structure of the P6/mmm space group. For the  $TiH_2$  powders, peaks of the  $TiH_{1.924}$  crystalline phase were identified with a cubic structure of the Fm-3m space group. The XRD spectrums were indexed according to the crystallographic data reports of the ICDD/JCPDS reference, PDF # 44-1294, 35-0741, and 25-0982 for  $Ti$ ,  $TiB_2$ , and  $TiH_{1.924}$  phases, respectively.



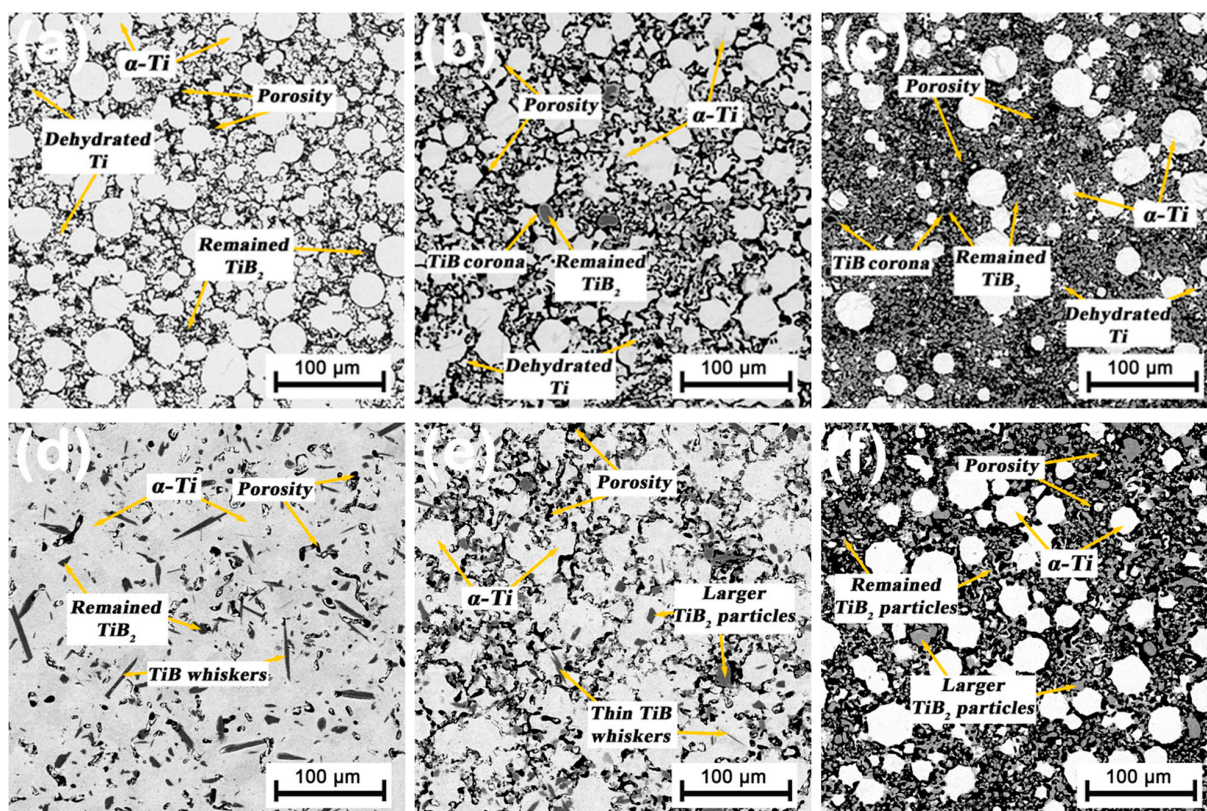
**Figure 1.** SEM micrographs of raw powders (a) CP-Ti Grade 1, (b)  $TiH_2$  grade VM, (c)  $TiB_2$  reinforcement particles, and (d) the XRD spectra as receive powders.

Figure 2 shows optical images of the microstructure of the sintered U samples. As can be noticed in this figure, the microstructure of samples consisted of the primary  $\alpha$ -Ti phase without the presence of residual  $TiH_2$  phases, indicating that the dehydrogenation was effectively attained with the isothermal steps at 550 and 700 °C. It has been reported that the dehydrogenation process of  $TiH_2$  is achieved between 600 to 700 °C [7,14]. The microstructure resulting from the U-a sample is characterized by still visible Ti particles and large clusters of sintered dehydrated Ti (from  $TiH_2$  raw particles) on the boundary regions of Ti particles. Unsintered Ti particles at 850 °C have a relationship with the size of the initial Ti raw powder: <45  $\mu m$  approximately. Irregular and large pores can be observed, Figure 2a. These microstructural observations confirm that using a higher sintered temperature than the  $\alpha \rightarrow \beta$  transus (880 °C), samples present an equiaxed microstructure of  $\alpha$ -Ti grains with an average grain size of 35  $\mu m$ , Figure 2b. The grain shape and size are related to the slow cooling rate used after the sintering process. Moreover, it has been reported that the usage of  $TiH_2$  enables the equiaxed microstructure formation of the primary  $\alpha$ -Ti phase; Chen et al. [14] reported that in a high vacuum environment, the dehydrogenation of a single  $TiH_2$  particle produces a phase transformation from  $TiH_2$  to a primary  $\alpha$ -Ti phase. They found that  $TiH_2$  phase-out H gradually transformed into the primary  $\alpha$ -Ti phase by removing the residual hydrogen. Moreover, for this investigation, better densification of the samples is observed by a clear decrease in porosity as an effect of the use of higher sintering temperature, obtaining irregular pores at the grain boundaries. In addition, it is noticed that small size of porosities along the grain boundaries, and it was considered that such pores were performed before starting sintering by phase transformation (from  $TiH_2$  to Ti) during the dehydrogenation process; leading to an increase in grain size from  $40.87 \pm 16.36 \mu m$ , diameter, to  $57.98 \pm 7.63 \mu m$ , width, for the Ub and Uc sample, respectively. In the sintering structure at over 1300 °C (Figure 2c), the previously formed coarse pores were completely eliminated showing a Ti-like structure, but with a lamellar microstructure.



**Figure 2.** Optical micrographs for the microstructure of the unreinforced sintered samples at (a) U-a, (b) U-b and, (c) U-c.

Representative SEM images of R samples sintered at 850 and 1300 °C are shown in Figure 3. These images were obtained using a backscattered electron (BSE) filter in order to differentiate the presence of  $TiB_2$ -reinforced particles,  $\alpha$ -Ti phase, or even any residual  $TiH_2$  after the sintering process. As can be seen in Figure 3, the R3-a sample shows a similar microstructure to the U-a sample with a small amount of remaining  $TiB_2$  reinforcing particles and a considerable porosity. Moreover, sample R10-a displays a slight concentration of dehydrogenated Ti structures sintered in the grain boundary of the un-sintered Ti particles, and an incomplete chemical reaction of agglomerated remaining  $TiB_2$  particles with Ti and dehydrogenated Ti is observed forming  $TiB$  coronas surrounding the  $TiB_2$  particles, as observed in Figure 3b. Falodun et al. [33] attributed this behavior to the experimental conditions chosen such as temperature, boron concentration, and sintering time; when an interrupted chemical reaction between  $TiB_2$  and Ti particles occurred, some semi-reacted  $TiB_2$  particles are surrounded by  $TiB$  coronas phase, remaining in the microstructure as shown in Figure 3b. Furthermore, the high-volume fraction of  $TiB_2$  particles used in the R30-c sample is observed as a uniform distribution of un-reacted  $TiB_2$  particles, surrounding the un-sintered Ti particles, connected like a network (Figure 3c). The same microstructure was found by Izui H et al. [34], for composites of 10 and 20 vol.% of  $TiB_2$  particles sintered by the SPS sintering process under vacuum conditions at 900 °C. They identified  $TiB$  clusters distributed uniformly in the  $Ti$ - $TiBw$  phases, similar to the present work.



**Figure 3.** Microstructures of the R samples with the different reinforcement conditions after sintering. (a) R3-a, (b) R10-a and, (c) R30-a, (d) R3-c, (e) R10-c and, (f) R30-c samples.

On the other hand, the formation of  $TiB$  whiskers structures was observed for R3-c and R10-c samples as a result of the reaction between the matrix and  $TiB_2$  reinforcement particles (Figures 3d and 3e, respectively). As can be seen,  $TiB$  whiskers are observed with a uniform distribution in the  $\alpha$ -Ti microstructure. According to the phase diagram Ti-B [28,29], the formation of the  $TiB$  phase can be achieved through the following reaction:



The Reaction (3) occurs during the diffusion of  $B$  atoms into the titanium lattice through the vacancy mechanism, which is enhanced by the contribution of the vacancies produced by  $H$  release. Hence,  $TiB$  whiskers can be formed as long as the boron concentration in the reaction zone, around  $TiB_2$  particles, is less than 18 wt.% of boron, since there exists an excess of Ti and short sintering times will be used, delaying the diffusion process [19]. The whisker's lengths remain constant although widths increase slightly, for the R3-c sample. In this context, the primary whiskers formed in the R3-c sample had an average length of 34  $\mu m$  and a width of 5  $\mu m$  (aspect ratio~7), whereas the thin whiskers are 9.5  $\mu m$  average length and a width of 1.5  $\mu m$  (aspect ratio~6). Figure 3e shows the microstructure for the R10-c sample. In this figure, needle-shaped  $TiB$  whiskers can be observed uniformly distributed in the matrix of the sample. Whiskers have an average length and width of 15 and 1.5  $\mu m$  (aspect ratio~10), respectively, with thinner whiskers regions than the R3-c sample. In addition, larger remaining  $TiB_2$  particles with an average diameter of approximately 13  $\mu m$  are uniformly distributed in the  $\alpha$ -Ti microstructure can be detected in Figure 3e. Moreover, Figure 3f shows the effect of the high volume fraction of the reinforcement particles in the  $\alpha$ -Ti microstructure for the R30-c sample; as sintering temperature and the boron concentration rises (more than 18 wt.%) the whiskers can not be formed and only agglomerated of remained  $TiB_2$  particles were found, similar with Figure 3c.

Furthermore, a noticeable change is observed in the densification of the R compounds, Figure 3; the R3-c sample presents the lowest porosity than the R samples, because of the small amount of  $TiB_2$  particles, sintering temperature, the diffusion of  $B$  atoms in  $TiB$  by a vacancy mechanism and the release of hydrogen (Figures 3 and 4). A higher porosity level is observed when the concentration of reinforcing particles is increased to 30 vol.% (R-30 samples) as compared to the U samples, hence the density of the R samples drops 7, 17 and 26% average for 850, 1100, and 1300  $^{\circ}C$ , respectively (Figure 4).

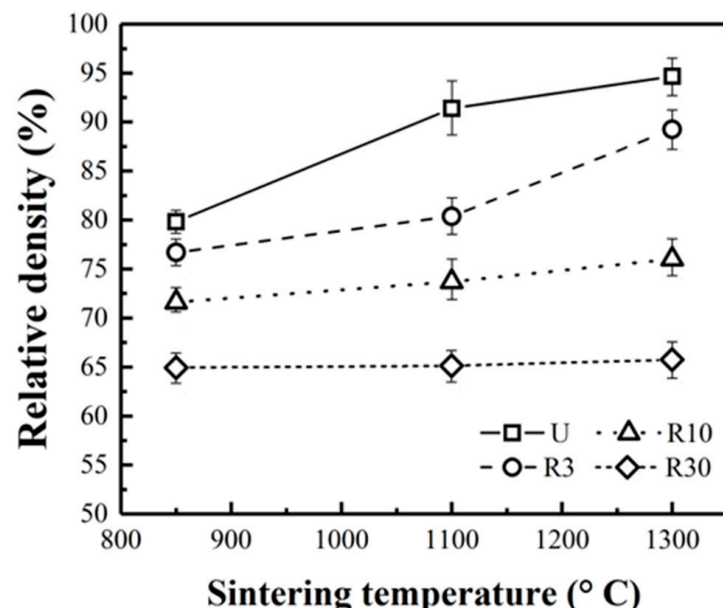


**Figure 4.** Densities for the set of experimental conditions, based on the  $Ti-TiH_2$  powders and  $TiB_2$  reinforcement particles.

To verify the composition of the U and R samples, a semiquantitative analysis from selected areas of the U- and R-c samples have been performed and presented in Figure 5. EDS results confirmed the whole  $Ti$  concentration (for the U-c sample) and the  $B$  concentration (for the R-c samples), as seen on the obtained microstructures in Figures 2 and 3. For the U-c sample, only  $Ti$  concentration can be achieved with a lamellar-shaped microstructure, confirming the dehydrogenation process and the presence of the primary  $\alpha$ -Ti phase as

described in the XRD section. Moreover, it is observed that by increasing the amount of  $B$ , the size of precipitates also increased; as reported by C. Arévalo et al. [35]. Thus, reinforced samples showed a major concentration of  $Ti$  as the main constituent of the matrix with the presence of  $B$ -enriched zones (remaining and large  $TiB_2$  particles). The preferential formation of needle-shaped  $TiB$  whiskers was identified for the R3-c sample (Figure 5b) with larger  $TiB_2$  particles. As seen in Figure 5b,c, some unreacted  $TiB_2$  particles are present in the final microstructure of samples. Moreover, several factors such as the increment of the  $TiB_2$  concentration, the diffusion phenomena, and the sintering temperature avoid the formation of  $TiB$  whiskers in R30 samples thus, only disseminated and large particles of  $TiB$  and  $TiB_2$  remained in the microstructure (as seen on Figures 3 and 5). Several PM processes of  $Ti-TiB_2$  composites reported the same behavior, when increasing the  $B$  concentration, the reaction products between them ( $Ti$  and  $TiB_2$ ) produce  $TiB$  phase formation [19]. This may be due to the excess titanium present in the system, as previously mentioned.

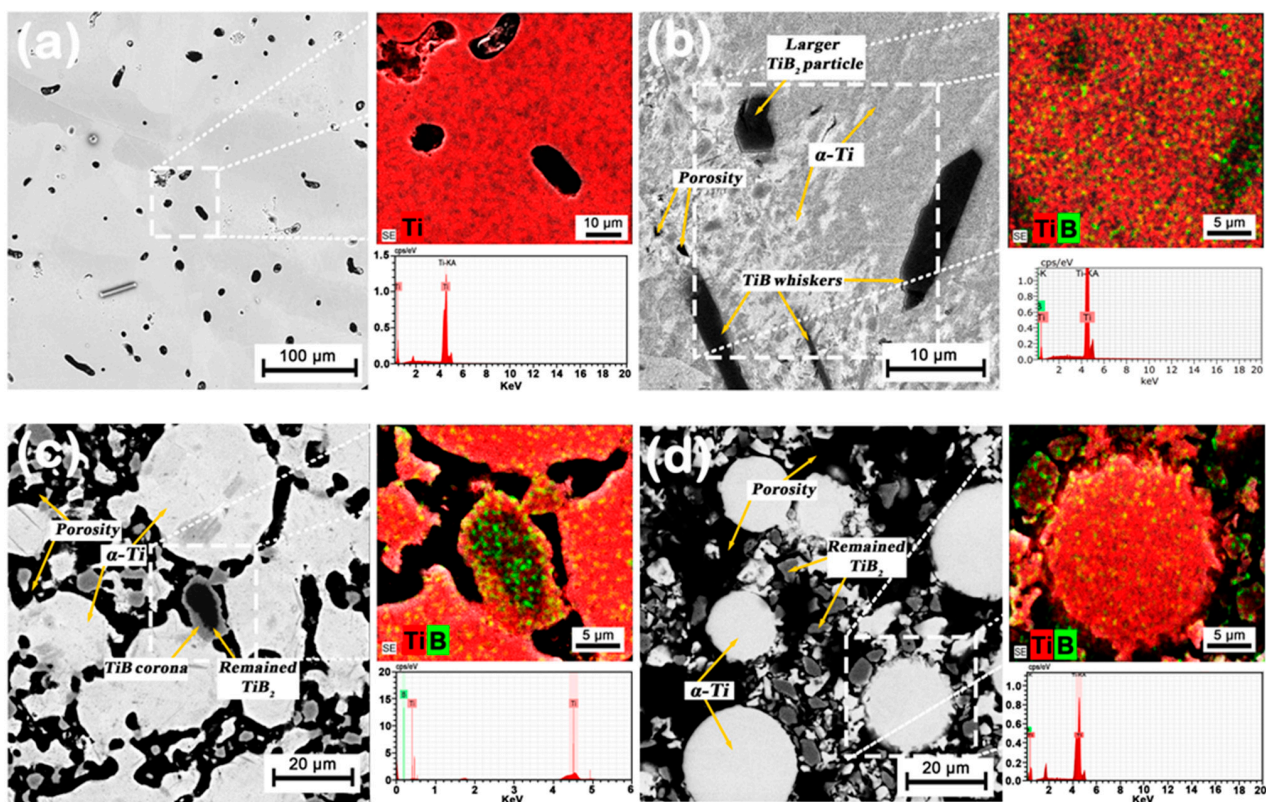


**Figure 5.** EDS analysis results for (a) U-c, (b) R3-c, (c) R10-c, and (d) R30-c samples.

XRD diffraction patterns of samples are shown in Figure 6a to Figure 6c, starting with  $Ti$ , as received powders ( $Ti$  AR) pattern (blue pattern) was added to compare the evolution of the  $\alpha-Ti$  phase. U samples exhibit the presence of  $\alpha-Ti$  phase peaks for the three sintering temperatures used in this investigation, similar to the  $Ti$  AR powder.  $\alpha-Ti$  phase peaks were identified by PDF # 44-1294, ICDD/JCPDS reference. The absence of  $TiH_2$  peaks in patterns of the sintered samples indicates that the hydrogen was effectively removed during the dehydrogenation process and only  $\alpha-Ti$  peaks for the sintered U samples were found. Furthermore, for the R samples, the higher intensity of  $\alpha-Ti$  peaks indicates that the matrix material is the main component of the samples. Peaks clearly indicate that the reinforcement particles and sintering temperature used induce the precipitation of the  $TiB$  intermetallic compound from the saturated  $\alpha-Ti$  solid solution, indicating that the temperature reaction was following the reaction in Equation (1). Moreover, the  $TiB$  and  $TiB_2$  phases are observed in patterns of R samples and indexed according to the crystallographic data reports of the ICDD/JCPDS reference (PDF # 05-0700 and 35-0741 for  $TiB$  and  $TiB_2$

phases, respectively); the presence of those phases is in agreement with the *Ti-B* phase diagram [28,29]. The intensity of  $TiB$  and  $TiB_2$  peaks increases with the amount of  $TiB_2$  reinforcement particles and the sintering temperature. This fact demonstrates the shrinkage of the  $Ti$  lattice with the reinforcement addition.

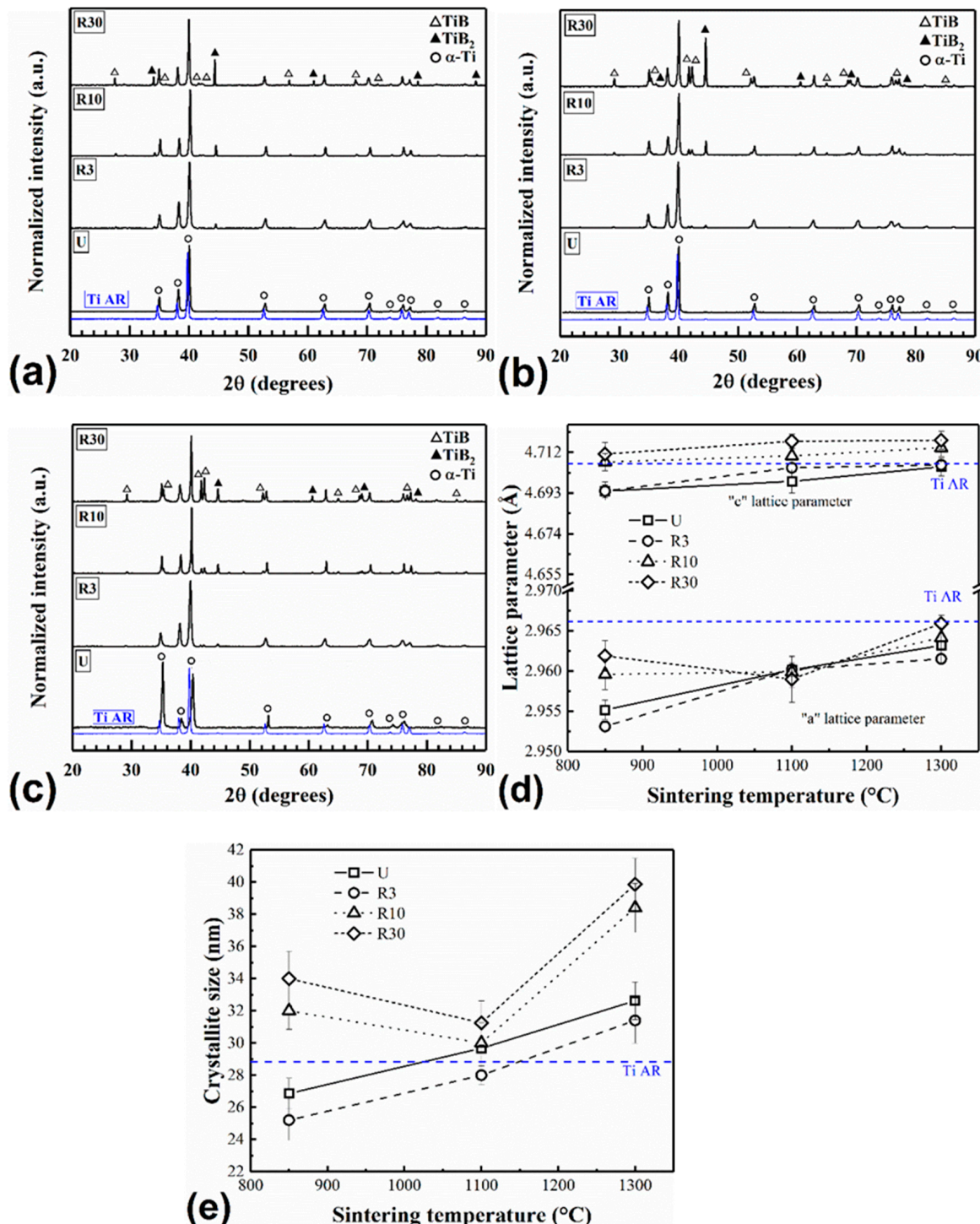


**Figure 6.** XRD patterns for the U and R samples after sintering at: (a) 850, (b) 1100 and, (c) 1300 °C; (d) lattice parameters, and (e) crystallite size of  $\alpha$ - $Ti$  for U and R samples as a function of the sintering temperature.

Figure 6d shows the evolution of the  $\alpha$ - $Ti$  solid solution lattice parameter size after the sintering process, estimated by Cohen's method [30]. The "c" lattice parameter slightly

increases when the sintering temperature increases. The U and R3 samples exhibit less deformation in comparison with the *Ti* AR powder (16 and 10%, respectively), by contrast, R10 and R30 samples display more deformation as compared with the “c” lattice parameter of the *Ti* AR powder (8 and 18%, respectively). The “a” lattice parameter for the set of the experimental conditions has a lower deformation in comparison with the *Ti* AR “a” parameter (under 2.9768 Å), with a small drop of the R10 and R30 samples at 1100 °C (around 2.960 Å, for the U and R samples as well). Those results can be expected since it is well established that incorporating *B* in substitutional positions in the HCP structure of *Ti* shrinks the unit cell [35,36], even demonstrating that the saturated  $\alpha$ -*Ti-TiH<sub>2</sub>* solid solution losses *H* due to the dehydrogenated reaction and the formation of the *TiB* phase due to the reaction in the Equation (1) during the PM sintering process. The lattice parameters of the  $\alpha$ -*Ti* solid solution after the PM process are greater than those of pure *Ti* (*a* = 2.951 and *c* = 4.684 Å) [37]. It is known that Boron atoms incorporated into the *Ti* structure result in more “c” lattice parameter expansion (over “a” parameter) due to anisotropic strain in the crystal lattice produced by the incorporation of *B* atoms in the interstices of the *Ti* structure.

The average crystallite size was estimated from XRD patterns by means of the modified Scherrer equation. As seen in Figure 6e, the crystallite size for the U and R3 samples linearly increases when it increases the sintering temperature (from 26.85 and 25.2 to 32.65 and 31.4 nm for the U and R3 samples, respectively), remaining slightly constant at 1100 °C compare with the crystallite size of the *Ti* AR powder (28.83 nm). Then, as *TiB<sub>2</sub>* concentration increases (R10 and R30 samples) crystallite sizes do at 850 °C, drop at 1100 °C because of the compression deformation caused by the “a” lattice parameter until 32 nm approximately, and finally increases when the sintering temperature rises at 1300 °C (38.4 and 39.85 nm for the R10 and R30 samples, respectively), up to the crystallite size of the *Ti* AR powder. Hence, this behavior indicates nearly random nucleation and growth of the *TiB* and *TiB<sub>2</sub>* phases in the *Ti* matrix; as the sintering temperature increases (with high accumulated energy from the PM sintering process) quickly recrystallize from 850 to 1300 °C and then grows slightly linearly, due to precipitation of *TiB* growth through the vacancies diffusion effect [38]. The apparent crystallite size for the set of experimental conditions did not exceed 100 nm.

Figure 7 shows the microhardness Vickers measured as a function of *TiB<sub>2</sub>* particle addition. Microhardness values for the U samples increased from 319 to 387 HV when the sintering temperature increased from 850 to 1300 °C, respectively. Microhardness values resulted as 28% higher as compared to the CP *Ti* microhardness values reported for *Ti* materials processed by PM [13,14,39] and 7% lower than values obtained at 1300 °C of sintered 100 % *TiH<sub>2</sub>* starting powders by PM process [13]. The difference between the reported results and those obtained in this investigation is attributed to the predominant equiaxed microstructure, as well as the reduction in the final porosity of U samples, which was promoted by grain growth, increasing the density of composites. Furthermore, microhardness values for R samples resulted in higher than the microhardness values of U samples, which increased with the volume fraction of the *TiB<sub>2</sub>* particles. The microhardness for the R10 and R30 samples increased until reaching relatively constant values around 500 HV. Microhardness values obtained in this investigation were 122 and 112% higher than those achieved for a *Ti* matrix reinforced with 2.5 and 5 vol.% of amorphous Boron sintered by inducive Hot Presing (iHP) process at 1100 and 1300 °C [35]. On the other hand, microhardness values obtained by the SPS process at 900 °C, with the usage of *TiB<sub>2</sub>* reinforcement particles (10 vol.%) and hydride-dehydride powders (balance) [34], can be compared with those obtained between 850 and 1100 °C in the present work; the microhardness values obtained in this work are higher than those reported by Izui H et al. (400 HV) [34] improving hardness values around 20% for the R10 sample obtained here (481 HV approximately, interpolating between 850 and 1100 °C). The hardness difference can be attributed because boron from reinforcement particles dissolves into the matrix (as *B* takes the places of *H* released and interstitial defects as well, through the vacancy diffusion mechanism). Hence the deformation presented in the lattice parameters (as seen in Figure 6d) can be attributed

to the sintering temperature and the addition of the  $TiB_2$  particle concentration; which had a major role in the microhardness rather than sample densification.

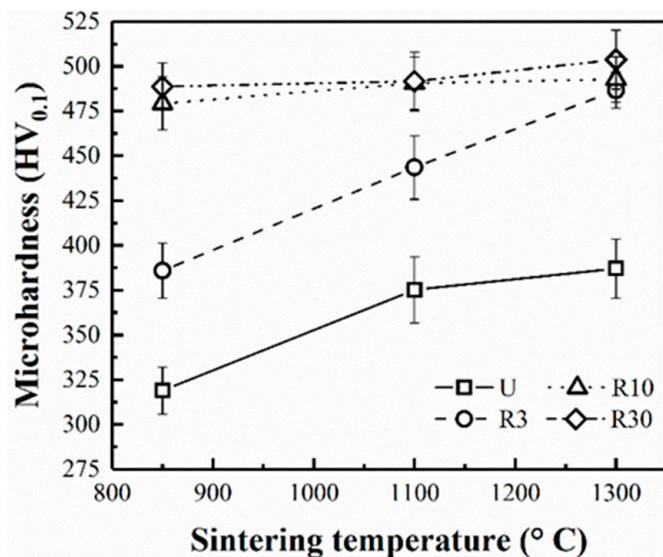


**Figure 7.** Microhardness Vickers versus sintering temperature for the set of experimental conditions.

Characteristic indentation load-depth nanoindentation curves for the U-c and R-c samples, using a maximum indentation load of 50 mN are depicted in Figure 8. The elastoplastic properties of the U and R samples, such as nanohardness ( $H$ ) and reduced Elastic modulus ( $E_r$ ) were determined by analyzing the indentation load-depth data according to the Oliver and Pharr procedure [32]; results are summarized in Table 2. The nano hardness values of the U samples increased up to 22.53% using the higher sintering temperature (1300 °C), regarding the values of the sample sintered at 850 °C (similar behavior as compared with Figure 7). This improvement can be attributed to the formation of pure  $TiB$  single crystals in the titanium matrix [26]. Compared with the U samples, nano hardness values for the R-a and R-c samples were improved as an effect of the addition of the  $TiB_2$  particles. Increments of 13% and 6% were attained for the R3-a and the R30-c samples, respectively. Clearly, the content of the reinforcement particles and secondary phases contribute to the hardening effect.

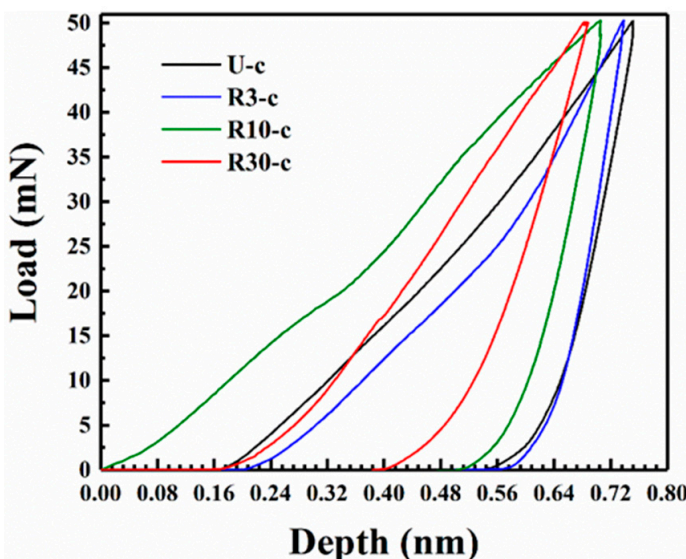


**Figure 8.** Characteristic nanoindentation curves load vs. depth, for U- and R-c samples.

**Table 2.** Nanoindentation values for the set of the experimental sintering process.

Sample	Depth $h_c$ (nm)	H (GPa)	$E_r$ (GPa)	$H/E_r$ [ $\times 10^{-2}$ ]	$H^3/E_r^2$ [ $\times 10^{-3}$ ] (GPa)
U-a	$858.05 \pm 65.85$	$3.61 \pm 0.53$	$101.77 \pm 9.54$	$3.55 \pm 0.04$	$4.54 \pm 0.23$
R3-a	$830.12 \pm 75.40$	$4.10 \pm 0.41$	$101.05 \pm 4.87$	$4.06 \pm 0.08$	$6.75 \pm 0.28$
R10-a	$798.72 \pm 73.98$	$4.48 \pm 0.43$	$100.14 \pm 7.23$	$4.47 \pm 0.04$	$9.97 \pm 0.32$
R30-a	$791.33 \pm 14.51$	$4.56 \pm 0.51$	$99.38 \pm 2.62$	$4.59 \pm 0.01$	$9.60 \pm 0.35$
U-b	$757.00 \pm 45.99$	$4.48 \pm 0.53$	$106.48 \pm 10.16$	$4.21 \pm 0.04$	$7.93 \pm 0.28$
R3-b	$730.05 \pm 58.90$	$4.86 \pm 0.48$	$105.57 \pm 2.83$	$4.60 \pm 0.05$	$10.30 \pm 0.30$
R10-b	$726.37 \pm 60.24$	$4.68 \pm 0.43$	$102.92 \pm 10.12$	$4.55 \pm 0.04$	$9.68 \pm 0.26$
R30-b	$721.13 \pm 15.05$	$4.74 \pm 0.25$	$101.27 \pm 9.49$	$4.68 \pm 0.02$	$10.38 \pm 0.16$
U-c	$817.10 \pm 83.95$	$4.66 \pm 0.43$	$108.05 \pm 5.39$	$4.31 \pm 0.04$	$8.67 \pm 0.24$
R3-c	$718.40 \pm 55.93$	$4.72 \pm 0.47$	$105.07 \pm 0.66$	$4.49 \pm 0.05$	$9.53 \pm 0.28$
R10-c	$711.70 \pm 16.90$	$4.85 \pm 0.23$	$103.39 \pm 10.23$	$4.69 \pm 0.02$	$10.67 \pm 0.15$
R30-c	$703.65 \pm 65.51$	$4.94 \pm 0.49$	$104.76 \pm 10.12$	$4.72 \pm 0.04$	$10.98 \pm 0.32$

As can be seen in Table 2, the  $E_r$  values of samples slightly decreased with the reinforcement particle addition, following the trend of the nano hardness. For example, the  $E_r$  for the R-b samples decreases 0.9, 3.4 and, 4.8% in comparison with the U-b sample. In this case, the increase in sintering temperature and  $TiB_2$  concentrations affects the enhancement of the nano hardness than the reduced Elastic modulus of the compounds. In literature, the  $E_r$  values for SML-fabricated CP-Ti and Ti-TiB composite are in the range of 102–134 GPa and 110–153 GPa, respectively, [22,41] that exhibit close to those values obtained in the present work.

On the other hand, the identification of  $TiB_2$  and  $TiB$  particles by means of XRD, SEM, and EDS analysis allowed us to essay these zones in order to evaluate their elastoplastic properties. The  $H$  and  $E_r$  for the  $TiB$  and  $TiB_2$  phases evaluated in this work resulted similarly to the values reported in the literature [21,33,42]. Moreover, nanoindentation assays were performed to confirm the presence of  $TiB$  and  $TiB_2$  phases. Those values resulted similarly to values found in other studies [40,42], around 15 and 27 GPa for  $TiB$  and  $TiB_2$  phases, respectively.

In addition to nanohardness and reduced Elastic modulus, nanoindentation essays are also useful to assess the wear resistance of a material, which can be used to predict the service life of a component [41,43]. Classical theories of wear show that nano hardness is a key parameter in controlling the wear resistance of a material [43]. In literature, concerning nanoindentation essays, the wear of a material can be described by the  $H/E_r$  and the  $H^3/E_r^2$  ratios [41,43]. The  $H/E_r$  ratio is related to the ability to resist elastic strain to failure; a combination of high nano hardness against reduced Elastic modulus often indicates good wear properties.  $H^3/E_r^2$  is referred to as yield pressure; as higher as much is this parameter indicates more resistance to plastic deformation [41,43]. Consequently, these parameters can be used to gauge the anti-wear ability of materials, as the wear caused by the gradual removal of material is associated with plastic deformation. In this work, the  $H$  and  $E_r$  to estimate the  $H/E_r$  and the  $H^3/E_r^2$  ratios (as seen in Table 2) for the sintered U and R samples. The resultant values are around (0.0397 to 0.0431 and 0.00454 to 0.0087 GPa for the U samples, respectively) and (0.041 to 0.047 and 0.00675 to 0.0109 GPa for the R samples, respectively) indicating a higher wear resistance for the R samples than the U samples. Nevertheless, these two ratios are higher than the literature  $H$  and  $E_r$  values of the CP-Ti biomaterial (0.0238 and 0.0014 GPa) [41], even though the  $H$  and  $E_r$  values of  $Ti-Fe-Ta$  alloys obtained by the casting process (0.0375 to 0.0455 and 0.0045 to 0.0115 GPa, respectively) [43] and the  $Ti-B$  composite materials produced by selective laser melting of 5 wt.% of  $TiB_2$  powders (0.030 and 0.004 GPa, respectively) [41]; indicating that the U and R samples designed here exhibit better wear behavior.

#### 4. Conclusions

The microstructure of the  $Ti-TiH_2$  matrix samples was characterized by equiaxed grains and gross lamellar structures. XRD and EDS analysis confirmed the presence of the  $\alpha$ - $Ti$ ,  $TiB$ , and  $TiB_2$  phases without the presence of residual  $TiH_2$  phase in the compounds. The diffusion between  $Ti$  and the reinforcing particles ( $TiB_2$ ) allowed the formation of the intermetallic  $TiB$  phase in the R samples. The presence of whisker structures was observed for the R3-c and R10-c samples, which was promoted by the amount concentration of the  $TiB_2$  particles, the sintering temperature, and the excess of titanium. The grain boundary is made of a clean  $\alpha$ - $Ti$  structure and thus is accompanied by grain growth, which increases the sintered relative density for the U samples (to 95%) and decreases up to 65% when the sintering temperature and the amount of  $TiB_2$  particles increases.

Vickers microhardness values increased with both the sintering temperature and the amount of  $TiB_2$  reinforcing particles, attaining a microhardness value of  $\approx 500$  HV0.1. Through nanoindentation tests, the nano hardness of samples increased with the  $TiB_2$  particle amount and the sintering temperature, while the reduced Elastic modulus was slightly reduced. Higher  $H/E_r$  and  $H^3/E_r^2$  ratios of the R samples exhibit better wear resistance than unreinforced samples and commercially used CP- $Ti$ . This demonstrates that the compounds generated in this work show better behavior to be considered for biomedical applications and it is more suitable than CP- $Ti$ .

**Author Contributions:** D.I.B.B., Writing original draft preparation—Formal analysis—Conceptualization; J.M.C.A., Writing—Formal analysis—Investigation; O.J.A., Conceptualization—Resources—Writing review and editing—Project administration; L.O.N., Visualization—Validation; M.F.F.J., Methodology—Data curation—Investigation; M.A.G.A., Formal analysis—Investigation—Visualization; I.G.F.V., Resources—Conceptualization—Investigation. All authors have read and agreed to the published version of the manuscript.

**Funding:** This work was supported by the National Council of Science and Technology (CONACyT) [grants Cátedras 348 and CB-1217-2018-11813] and State Council of Science and Technology of Jalisco (COECyTJAL) [grant 8205-2019].

**Institutional Review Board Statement:** Not applicable.

**Informed Consent Statement:** Not applicable.

**Data Availability Statement:** The data presented in this study are available on request from the corresponding author. The data are not publicly available due to the extremely large size.

**Acknowledgments:** The authors thank the Mexican Council of Science and Technology (CONACyT) and the University of Guadalajara for the support received during the development of this research. This work was supported by Cátedras-CONACyT project 348, research grants CB-2017-11813 and 8205-2019 of the CONACyT and COECyTJAL, respectively.

**Conflicts of Interest:** The authors declare no conflict of interest.

#### References

1. Brunette, D.M.; Tengvall, P.; Textor, M.; Thomsen, P. *Titanium in Medicine*; Engineering Materials; Springer: Berlin/Heidelberg, Germany, 2001; ISBN 978-3-642-63119-1.
2. Hiromoto, S.; Mischler, S. The Influence of Proteins on the Fretting–Corrosion Behaviour of a Ti6Al4V Alloy. *Wear* **2006**, *261*, 1002–1011. [[CrossRef](#)]
3. Hao, Y.L.; Li, S.J.; Sun, S.Y.; Zheng, C.Y.; Yang, R. Elastic Deformation Behaviour of Ti-24Nb-4Zr-7.9Sn for Biomedical Applications. *Acta Biomater.* **2007**, *3*, 277–286. [[CrossRef](#)]
4. Leyens, C.; Peters, M. *Titanium and Titanium Alloys*; Leyens, C., Peters, M., Eds.; Wiley: Hoboken, NJ, USA, 2003; ISBN 9783527305346.
5. Niinomi, M. Mechanical Properties of Biomedical Titanium Alloys. *Mater. Sci. Eng. A* **1998**, *243*, 231–236. [[CrossRef](#)]
6. Froes, F.H. Powder Metallurgy of Titanium Alloys. In *Advances in Powder Metallurgy*; Elsevier: Amsterdam, The Netherlands, 2013; pp. 202–240.
7. Ivasishin, O.M.; Eylon, D.; Bondarchuk, V.I.; Savvakin, D.G. Diffusion during Powder Metallurgy Synthesis of Titanium Alloys. *Defect Diffus. Forum* **2008**, *277*, 177–185. [[CrossRef](#)]
8. Sharma, B.; Vajpai, S.K.; Ameyama, K. Preparation of Strong and Ductile Pure Titanium via Two-Step Rapid Sintering of  $TiH_2$  Powder. *J. Alloys Compd.* **2016**, *683*, 51–55. [[CrossRef](#)]

9. Amherd Hidalgo, A.; Frykholm, R.; Ebel, T.; Pyczak, F. Powder Metallurgy Strategies to Improve Properties and Processing of Titanium Alloys: A Review. *Adv. Eng. Mater.* **2017**, *19*, 1600743. [[CrossRef](#)]
10. Wysocki, B.; Maj, P.; Krawczyńska, A.; Rożniatowski, K.; Zdunek, J.; Kurzydłowski, K.J.; Święzkowski, W. Microstructure and Mechanical Properties Investigation of CP Titanium Processed by Selective Laser Melting (SLM). *J. Mater. Process. Technol.* **2017**, *241*, 13–23. [[CrossRef](#)]
11. Shon, J.; Park, J.; Cho, K.; Hong, J.; Park, N.; Oh, M. Effects of Various Sintering Methods on Microstructure and Mechanical Properties of CP-Ti Powder Consolidations. *Trans. Nonferrous Met. Soc. China* **2014**, *24*, s59–s67. [[CrossRef](#)]
12. Zhang, Y.; Wang, C.; Liu, Y.; Liu, S.; Xiao, S.; Chen, Y. Surface Characterizations of TiH<sub>2</sub> Powders before and after Dehydrogenation. *Appl. Surf. Sci.* **2017**, *410*, 177–185. [[CrossRef](#)]
13. Lee, D.-W.; Lee, H.-S.; Park, J.-H.; Shin, S.-M.; Wang, J.-P. Sintering of Titanium Hydride Powder Compaction. *Procedia Manuf.* **2015**, *2*, 550–557. [[CrossRef](#)]
14. Chen, G.; Liss, K.D.; Auchterlonie, G.; Tang, H.; Cao, P. Dehydrogenation and Sintering of TiH<sub>2</sub>: An In Situ Study. *Metall. Mater. Trans. A Phys. Metall. Mater. Sci.* **2017**, *48*, 2949–2959. [[CrossRef](#)]
15. Bhosle, V.; Baburaj, E.G.; Miranova, M.; Salama, K. Dehydrogenation of TiH<sub>2</sub>. *Mater. Sci. Eng. A* **2003**, *356*, 190–199. [[CrossRef](#)]
16. Chávez, J.; Olmos, L.; Jiménez, O.; Bouvard, D.; Rodríguez, E.; Flores, M. Sintering Behaviour and Mechanical Characterisation of Ti64/xTiN Composites and Bilayer Components. *Powder Metall.* **2017**, *60*, 257–266. [[CrossRef](#)]
17. Gogotsi, Y.G.; Andrievski, R.A. (Eds.) *Materials Science of Carbides, Nitrides and Borides*, 1st ed.; Springer Science + Business Media Dordrecht: St. Petersburg, Russia, 1999; ISBN 978-0-7923-5707-0.
18. Zhang, X.; Lü, W.; Zhang, D.; Wu, R.; Bian, Y.; Fang, P. In Situ Technique for Synthesizing (TiB+TiC)/Ti Composites. *Scr. Mater.* **1999**, *41*, 39–46. [[CrossRef](#)]
19. Morsi, K.; Patel, V.V. Processing and Properties of Titanium-Titanium Boride (TiBw) Matrix Composites—A Review. *J. Mater. Sci.* **2007**, *42*, 2037–2047. [[CrossRef](#)]
20. Feng, H.; Zhou, Y.; Jia, D.; Meng, Q. Microstructure and Mechanical Properties of in Situ TiB Reinforced Titanium Matrix Composites Based on Ti-FeMo-B Prepared by Spark Plasma Sintering. *Compos. Sci. Technol.* **2004**, *64*, 2495–2500. [[CrossRef](#)]
21. Zhang, X.; Xu, Q.; Han, J.; Kvanin, V.L. Self-Propagating High Temperature Combustion Synthesis of TiB/Ti Composites. *Mater. Sci. Eng. A* **2003**, *348*, 41–46. [[CrossRef](#)]
22. Atri, R.R.; Ravichandran, K.S.; Jha, S.K. Elastic Properties of In-Situ Processed Ti-TiB Composites Measured by Impulse Excitation of Vibration. *Mater. Sci. Eng. A* **1999**, *271*, 150–159. [[CrossRef](#)]
23. Ma, Z.Y.; Tjong, S.C.; Gen, L. In-Situ Ti-TiB Metal-Matrix Composite Prepared by a Reactive Pressing Process. *Scr. Mater.* **2000**, *42*, 367–373. [[CrossRef](#)]
24. Kobayashi, M.; Funami, K.; Suzuki, S.; Ouchi, C. Manufacturing Process and Mechanical Properties of Fine TiB Dispersed Ti-6Al-4V Alloy Composites Obtained by Reaction Sintering. *Mater. Sci. Eng. A* **1998**, *243*, 279–284. [[CrossRef](#)]
25. Fan, Z.; Miodownik, A.P.; Chandrasekaran, L.; Ward-Close, M. The Young's Moduli of in Situ Ti/TiB Composites Obtained by Rapid Solidification Processing. *J. Mater. Sci.* **1994**, *29*, 1127–1134. [[CrossRef](#)]
26. Gorsse, S.; Chaminade, J.P.; Le Petitcorps, Y. In Situ Preparation of Titanium Base Composites Reinforced by TiB Single Crystals Using a Powder Metallurgy Technique. *Compos. Part A Appl. Sci. Manuf.* **1998**, *29*, 1229–1234. [[CrossRef](#)]
27. Ravi Chandran, K.S.; Panda, K.B.; Sahay, S.S. TiBw-Reinforced Ti Composites: Processing, Properties, Application Prospects, and Research Needs. *Jom* **2004**, *56*, 42–48. [[CrossRef](#)]
28. ASM International. *Alloy Phase Diagrams*; Okamoto, H., Schlesinger, M.E., Mueller, E.M., Eds.; ASM International: Almere, The Netherlands, 2016; Volume 3, ISBN 978-1-62708-163-4. [[CrossRef](#)]
29. Predel, B. B-Ti (Boron-Titanium). In *B-Ba-C-Zr*; Madelung, O., Ed.; Springer: Berlin/Heidelberg, Germany, 1992; pp. 1–3.
30. Cullity, B.D.; Weymouth, J.W. Elements of X-ray Diffraction. *Am. J. Phys.* **1957**, *25*, 394–395. [[CrossRef](#)]
31. Langford, J.I.; Wilson, A.J.C. Scherrer after Sixty Years: A Survey and Some New Results in the Determination of Crystallite Size. *J. Appl. Cryst.* **1978**, *11*, 102–113. [[CrossRef](#)]
32. Oliver, W.C.; Pharr, G.M. An Improved Technique for Determining Hardness and Elastic Modulus Using Load and Displacement Sensing Indentation Experiments. *J. Mater. Res.* **1992**, *7*, 1564–1583. [[CrossRef](#)]
33. Falodun, O.E.; Obadele, B.A.; Oke, S.R.; Okoro, A.M.; Olubambi, P.A. Titanium-Based Matrix Composites Reinforced with Particulate, Microstructure, and Mechanical Properties Using Spark Plasma Sintering Technique: A Review. *Int. J. Adv. Manuf. Technol.* **2019**, *102*, 1689–1701. [[CrossRef](#)]
34. Izui, H.; Oota, A.; Matsuura, K.; Kamegawa, S. Tensile Behavior of TiB-Reinforced Ti Matrix Composites with Different Titanium Powders. *Mech. Eng. J.* **2016**, *3*, 15-00571. [[CrossRef](#)]
35. Arévalo, C.; Montalegre-Meléndez, I.; Pérez-Soriano, E.; Ariza, E.; Kitzmantel, M.; Neubauer, E. Study of the Influence of TiB Content and Temperature in the Properties of In Situ Titanium Matrix Composites. *Metals* **2017**, *7*, 457. [[CrossRef](#)]
36. Sahay, S.S.; Ravichandran, K.S.; Atri, R.; Chen, B.; Rubin, J. Evolution of Microstructure and Phases in In Situ Processed Ti-TiB Composites Containing High Volume Fractions of TiB Whiskers. *J. Mater. Res.* **1999**, *14*, 4214–4223. [[CrossRef](#)]
37. Wood, R.M. The Lattice Constants of High Purity Alpha Titanium. *Proc. Phys. Soc.* **1962**, *80*, 783–786. [[CrossRef](#)]
38. Lifshits, I.M.; Slezov, V.V. Kinetics of the Diffusion Decomposition of Supersaturated Solid Solutions. *Zhurnal Eksperimental'noi Teor. Fiz.* **1958**, *35*, 479–492.

39. Diouf, S.; Durowoju, M.O.; Shongwe, M.B.; Olubambi, P.A. Processing of Pure Titanium Containing Titanium-Based Reinforcing Ceramics Additives Using Spark Plasma Sintering. *Leonardo Electron. J. Pract. Technol.* **2017**, *30*, 269–286.
40. Attar, H.; Ehtemam-Haghghi, S.; Kent, D.; Okulov, I.V.; Wendrock, H.; Bönisch, M.; Volegov, A.S.; Calin, M.; Eckert, J.; Dargusch, M.S. Nanoindentation and Wear Properties of Ti and Ti-TiB Composite Materials Produced by Selective Laser Melting. *Mater. Sci. Eng. A* **2017**, *688*, 20–26. [[CrossRef](#)]
41. Atar, E.; Kayali, E.S.; Cimenoglu, H. Characteristics and Wear Performance of Borided Ti6Al4V Alloy. *Surf. Coat. Technol.* **2008**, *202*, 4583–4590. [[CrossRef](#)]
42. Munro, R.G. Material Properties of Titanium Diboride. *J. Res. Natl. Inst. Stand. Technol.* **2000**, *105*, 709. [[CrossRef](#)]
43. Ehtemam-Haghghi, S.; Cao, G.; Zhang, L.C. Nanoindentation Study of Mechanical Properties of Ti Based Alloys with Fe and Ta Additions. *J. Alloys Compd* **2017**, *692*, 892–897. [[CrossRef](#)]

**Disclaimer/Publisher’s Note:** The statements, opinions and data contained in all publications are solely those of the individual author(s) and contributor(s) and not of MDPI and/or the editor(s). MDPI and/or the editor(s) disclaim responsibility for any injury to people or property resulting from any ideas, methods, instructions or products referred to in the content.